Noncontact three-dimensional mapping of intracellular hydromechanical properties by Brillouin microscopy

Giuliano Scarcelli[1–3], William J Polacheck[4], Hadi T Nia[4], Kripa Patel[1], Alan J Grodzinsky[4–6], Roger D Kamm[4,5] & Seok Hyun Yun[1,2,7]

Current measurements of the biomechanical properties of cells require physical contact with cells or lack subcellular resolution. Here we developed a label-free microscopy technique based on Brillouin light scattering that is capable of measuring an intracellular longitudinal modulus with optical resolution. The 3D Brillouin maps we obtained of cells in 2D and 3D microenvironments revealed mechanical changes due to cytoskeletal modulation and cell-volume regulation.

The interaction between the liquid and solid phases in the cytoplasm regulates the rheological behavior of cells[1] and has a prominent role in determining how cells deform and move[2]. In turn, the hydromechanical properties of cells, such as the viscoelastic modulus and compressibility, influence intracellular water transport, cytoskeletal-network modulation and cell-volume regulation[3]. It is necessary to measure these properties *in situ* to study how cells regulate intracellular mechanics and how the properties change as cells interact with their microenvironment during aging and injury healing, as well as in the course of disease pathogenesis[4]. Mechanical techniques such as atomic force microscopy (AFM) and magnetic bead twisting have been widely used to measure the viscoelastic moduli and deformability of cells, and they have helped to elucidate the different mechanisms by which cells regulate mechanical properties such as cross-linking, branching and pre-stress in the cytoskeleton or variations in the solid-liquid volume fraction[5]. However, these techniques require contact with cells to impose mechanical stress, which limits their applicability to cells cultured on flat 2D substrates[6] or to micropatterned wells that maintain the 3D cell shape[7,8]. Optical tweezers or stretchers[9], micropipette aspiration[10] and microfluidic deformation assays[11] have been used to assess the elasticity of a cell in suspension, but without subcellular resolution. For cells that are confined in 3D hydrogels or microfluidic chips, particle-tracking microrheology[12] is potentially viable, but it requires the insertion of microbeads into cells and, if tracking subcellular components, it is influenced by motor activity[13]; furthermore, the resolution is limited by the number, size and random location distribution of the beads. Because of the limitations of these current methods, mapping of the mechanical properties of cells in a 3D meshwork of extracellular matrix proteins has not been performed yet[14]. As a result, there is a dearth of information on the biomechanical properties of cells in 3D environments and how they may differ from those of cells on a flat 2D substrate.

To address this need, we introduce Brillouin optical cell microscopy for noncontact, label-free and 3D mapping of intracellular and extracellular hydromechanical properties. This technique is based on the interaction of light with spontaneous acoustic phonons in the gigahertz frequency range[15]. By measuring the optical frequency shift of the scattered light, Brillouin measurements probe the local spontaneous pressure waves in intracellular environments, from which one can determine the high-frequency longitudinal modulus[16]. Mechanically, Brillouin interaction can be thought of as a test that measures the ratio of uniaxial stress to strain in confined compression conditions at high frequency[17] (**Supplementary Note 1** and **Supplementary Fig. 1**). The longitudinal modulus depends on intrinsic properties such as the modulus of individual cytoskeletal components, network cross-linking, the compressibility of the local microenvironment and the solid-liquid volume fraction (**Fig. 1a**). To enable cellular Brillouin mapping, we constructed a confocal Brillouin cell microscope by using a high–numerical aperture (0.6) objective lens that yields a spatial resolution of ~0.5 × 0.5 × 2 μm^3 and a nonscanning parallel Brillouin spectrometer based on our previous design[18], but with an enhanced spectral extinction of 70 dB, spectral resolution of 600 MHz and low loss (<10 dB) (**Fig. 1b**, **Supplementary Note 2** and **Supplementary Fig. 2**), as well as a spectrum calibration arm (**Supplementary Note 3** and **Supplementary Fig. 3**). The light source was a 532-nm continuous-wave laser. With optical power levels of 2–4 mW at the sample and a spectral acquisition time of 0.1–0.2 s, the frequency-measurement sensitivity of the instrument was ~10 MHz (**Supplementary Note 4** and **Supplementary Fig. 4**). This is about 0.1% of the Brillouin frequency shift of water (7.44 GHz at 18 °C).

To validate Brillouin microscopy for applications at the cellular scale, we investigated whether it is sensitive to liquid-solid regulation under different osmotic conditions. Adding sucrose to the cell medium generates osmotic pressure, which induces a substantial increase in cell elastic modulus[19]. Brillouin confocal sections of an

[1]Wellman Center for Photomedicine, Massachusetts General Hospital, Boston, Massachusetts, USA. [2]Department of Dermatology, Harvard Medical School, Boston, Massachusetts, USA. [3]Fischell Department of Bioengineering, University of Maryland, College Park, Maryland, USA. [4]Department of Mechanical Engineering, Massachusetts Institute of Technology, Cambridge, Massachusetts, USA. [5]Department of Biological Engineering, Massachusetts Institute of Technology, Cambridge, Massachusetts, USA. [6]Department of Electrical Engineering, Massachusetts Institute of Technology, Cambridge, Massachusetts, USA. [7]The Harvard-MIT Health Sciences and Technology Program, Cambridge, Massachusetts, USA. Correspondence should be addressed to G.S. (scarc@umd.edu) or S.H.Y. (syun@hms.harvard.edu).

RECEIVED 27 MARCH; ACCEPTED 27 AUGUST; PUBLISHED ONLINE 5 OCTOBER 2015; DOI:10.1038/NMETH.3616

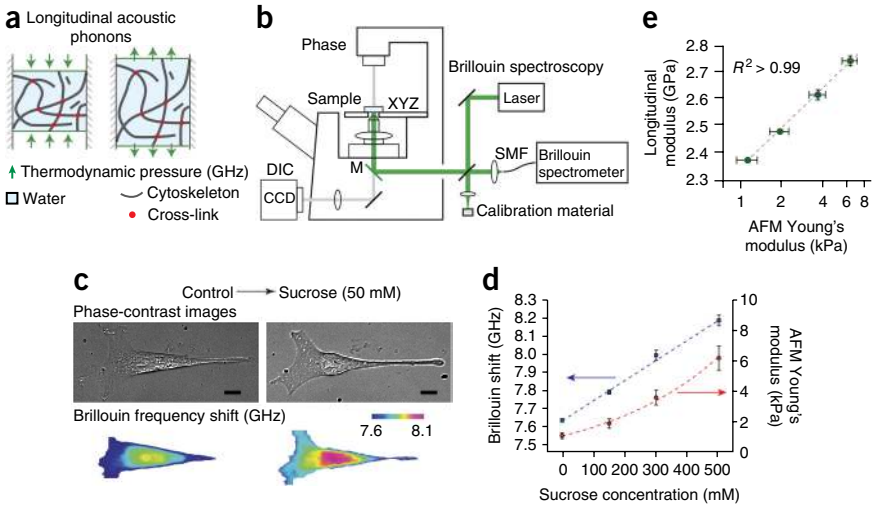

Figure 1 | Principle and validation of Brillouin microscopy. (**a**) Schematic of the mechanical interaction probed by Brillouin scattering. Spontaneous fluctuations in density and pressure behave as microscopic mechanical perturbations from which the longitudinal modulus can be extracted with high-resolution optical spectroscopy. (**b**) Schematic of the instrument. A standard fluorescence microscope was modified to introduce the Brillouin excitation beam; the Brillouin scattered light is collected and coupled into a fiber, which serves as a confocal pinhole. The fiber delivers light into the Brillouin spectrometer (**Supplementary Note 2** and **Supplementary Fig. 2**). DIC, differential interference contrast; CCD, charge-coupled device; SMF, single-mode fiber. (**c**) Brillouin images (and coregistered phase-contrast images) of a cell before and after hyperosmotic shock. Scale bars, 10 µm. (**d**) The effect of environmental osmolarity on both Brillouin and AFM-based micro-indentation measurements of cells. (**e**) Validation of Brillouin stiffness measurement against results of AFM-based micro-indentation tests for cells exposed to different levels of hyperosmotic shock. Each data point is the average of 8–11 measurements on different cells; error bars represent ±s.e.m.

NIH 3T3 cell before and after hyperosmotic shock (50 mM of sucrose) showed a notable increase in Brillouin shift throughout the cell (**Fig. 1c**). To compute the mean longitudinal modulus, we averaged the Brillouin shifts over the cell volume and used estimated constant values for cell density and refractive index[20]. This was an approximation, as refractive index and density are not uniform throughout cells and likely change under different osmotic conditions; however, we estimated that the changes in refractive index and density did not substantially affect the modulus estimation (**Supplementary Note 5** and **Supplementary Fig. 5**). The measured Brillouin shift varied linearly with the concentration of sucrose (**Fig. 1d**).

For comparison with the current gold standard for measurements of the Young's modulus of cells, we performed micro-indentation by using an atomic force microscope equipped with a 5-µm-diameter bead (**Supplementary Note 6** and **Supplementary Figs. 6–8**). The Young's modulus derived from the thin-layer Hertzian contact model of AFM indentation showed a nearly quadratic increase with sucrose concentration[1,19] (**Fig. 1d** and **Supplementary Fig. 6**). Typical values of the high-frequency longitudinal modulus are on the order of gigapascals, owing to the low compressibility of the intracellular microenvironment, and should not be interpreted as Young's or shear moduli of the cell, which are typically on the order of kilopascals when measured at low frequencies[6]. However, our data showed a high correlation ($R^2 > 0.99$) between the variations of these two types of moduli under the same environmental conditions (**Fig. 1e**). This result indicates that the underlying biochemical, physical and structural changes in the cell in response to the change in osmotic pressure affect both longitudinal and Young's moduli in the same direction. We have consistently observed such correlation in biological tissues[21], as well as for synthetic hydrogels (**Supplementary Note 7** and **Supplementary Fig. 9**). Furthermore, in hydrogels, Brillouin signatures are sensitive to mechanical changes due to both polymer concentration and polymer cross-linking (**Supplementary Fig. 10**). The log-log linear relationship between the longitudinal modulus M' and Young's modulus E' is expressed as $\log(M') = a\log(E') + b$, where a and b are material-dependent coefficients[21]. Our instrument was able to detect a 0.05% change in the longitudinal modulus, which corresponds to 2% change in Young's modulus. This sensitivity is similar to, if not better than, that of contact-based mechanical measurements.

Cytoskeleton modifications are important in the regulation of cell mechanical properties. Using reconstituted actin gels *in vitro*, we verified that the Brillouin frequency shift was sensitive to two major mechanisms of cytoskeleton stiffening: actin

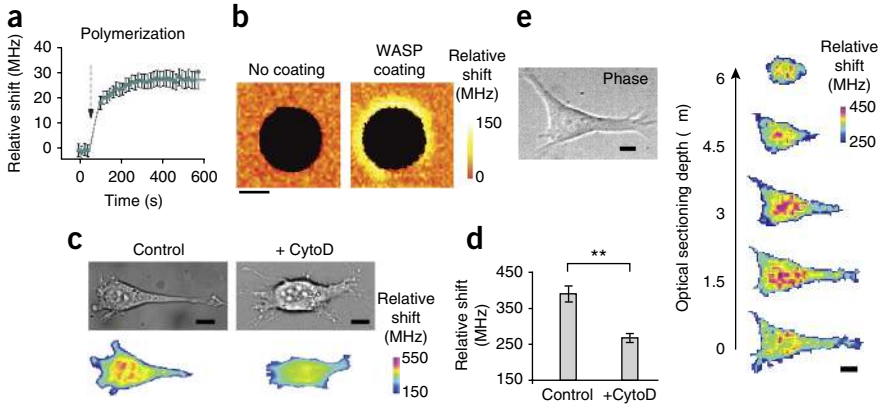

Figure 2 | Brillouin microscopy measurements of mechanical changes *in vitro* and in a cell. (**a**) Brillouin frequency shift during actin polymerization into a gel. Data shown are relative to the Brillouin shift of 7.44 GHz for pure water at room temperature. (**b**) Brillouin microscopy images of the mechanical changes around beads promoting actin branching. Scale bar, 5 µm. (**c**) Representative images of two different NIH 3T3 cells treated with cytochalasin D (+CytoD) or not treated (control). Scale bars, 10 µm. (**d**) A reduction in Brillouin shift was observed between cytochalasin D–treated cells ($N = 14$) and controls ($N = 13$) when values were averaged over the whole cell volume (**$P < 0.0001$, unpaired two-tailed t-test). (**e**) Three-dimensional confocal reconstruction of the intracellular stiffness in an NIH 3T3 fibroblast cultured on a 15-kPa polyacrylamide gel substrate. Scale bars, 10 µm. Error bars represent ±s.e.m. in **a** and **d**.

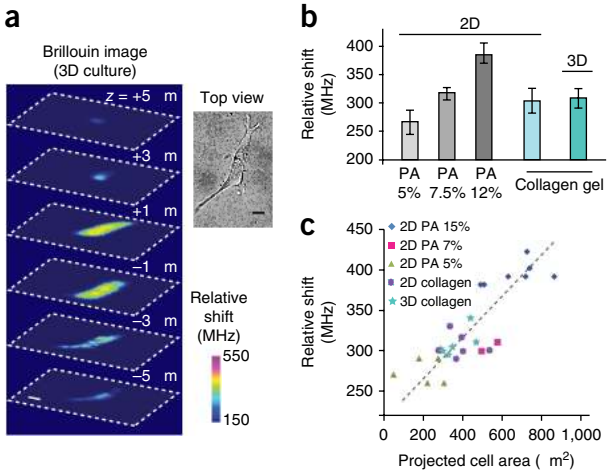

Figure 3 | Effect of the extracellular matrix on cell stiffness. (**a**) Representative 3D Brillouin image reconstruction of an NIH 3T3 cell cultured in a collagen gel matrix and the related top view obtained with bright-field microscopy ($N = 5$). Scale bars, 10 µm. (**b**) Average Brillouin shift of NIH 3T3 fibroblasts cultured on top of polyacrylamide (PA) gel substrates of (from left to right) ~1 kPa ($N = 8$), 2.5 kPa ($N = 8$) and 15 kPa ($N = 12$) and soft collagen gel substrates (~300 Pa) ($N = 5$) compared with the average Brillouin shift of cells cultured in 3D collagen gels ($N = 5$). Error bars represent ±s.e.m. (**c**) Average Brillouin shift of NIH 3T3 fibroblasts plotted against the projected cell area in the different 2D and 3D microenvironments. Each symbol represents an individual data point.

polymerization (**Fig. 2a**) and branching of actin fibers with high spatial and temporal resolution (**Fig. 2b**). The Brillouin shifts increased as cells were spread on a 2D substrate (**Supplementary Note 8** and **Supplementary Fig. 11**) and decreased when actin polymerization was inhibited with cytochalasin D (**Fig. 2c**,**d**). The confocal sectioning of Brillouin microscopy allowed us to analyze the longitudinal modulus with 3D resolution. The Brillouin images of an NIH 3T3 fibroblast cultured on a polyacrylamide gel substrate showed a stiffer nucleus and softer cytoplasm (**Fig. 2e**).

The noncontact nature of the Brillouin technique enables the mechanical measurement of cells in physiologic 3D collagen matrices (**Fig. 3a**). For direct comparison with cells in 2D, we measured cells grown on flat polyacrylamide substrates with shear moduli of 1, 2.5 and 15 kPa (**Fig. 3b**). Consistent with previous studies[22], we observed an increase in Brillouin shift with increasing substrate rigidity. The Brillouin shift from cells cultured in 3D collagen gels with a shear modulus of ~300 Pa was nearly identical to that of cells grown on top of the same collagen gels and was similar to those of cells grown on stiffer, 2.5-kPa polyacrylamide gels (**Fig. 3b**). Cells grown on polyacrylamide substrates with low moduli (~1 kPa) were partially rounded and not fully spread; in contrast, cells on 2D collagen gels and in 3D collagen gels (~300 Pa) appeared well spread. This morphological behavior has been attributed to the higher density of adhesion sites or the nonlinear elasticity of collagen gels[23,24]. We found a strong correlation ($P < 0.001$) between cell stiffness and projected cell area (**Fig. 3c**). The data obtained on 2D substrates and in 3D hydrogels in various conditions collapsed on a single trend of cell stiffness versus maximum projected cell area (**Fig. 3c**). This finding, together with the identical intracellular moduli in 2D and 3D collagen gels, might indicate that cellular stiffness is similarly regulated in both 2D and 3D.

In conclusion, Brillouin optical microscopy enables mapping of the longitudinal moduli of live cells both on 2D substrates and in 3D matrices. The longitudinal modulus may not be directly linked to the tension in the cytoskeletal network or the cortical contractility[25]. However, Brillouin technology is sensitive to the biomechanical changes in a cell caused by factors such as biopolymer content, polymerization, branching and liquid-solid volume fraction. Brillouin microscopy opens up new research avenues for the biomechanical investigation of cells and their microenvironment in 3D at subcellular resolution.

METHODS

Methods and any associated references are available in the online version of the paper.

Note: Any Supplementary Information and Source Data files are available in the online version of the paper.

ACKNOWLEDGMENTS

We thank A.C. Martin, F.M. Mason, E. Moeendarbary, M.C. Gather and K. Franze for helpful discussions, as well as H. Oda, K. Sawicki and K. Berghaus for help with hydrogel measurements. This work was supported in part by the National Institutes of Health (grants K25-EB015885 and R21-EY023043 to G.S.; grants R01-EY025454 and P41-EB015903 to S.H.Y.; and grant R33 CA174550 to R.D.K.), the National Science Foundation (grant CBET-0853773 to S.H.Y.) and a Human Frontier Science Program Young Investigator Grant (RGY0074/2013 to G.S.).

AUTHOR CONTRIBUTIONS

G.S. and S.H.Y. conceived the project. G.S., W.J.P., R.D.K. and S.H.Y. devised the research plan. G.S. developed the instrument and performed the experiments. W.J.P. and K.P. developed cell protocols and performed cell-related control measurements. H.T.N., W.J.P. and A.J.G. designed and performed indentation experiments. G.S., W.J.P. and S.H.Y. wrote the manuscript with input from all other authors.

COMPETING FINANCIAL INTERESTS

The authors declare no competing financial interests.

1. Moeendarbary, E. *et al. Nat. Mater.* **12**, 253–261 (2013).
2. Stroka, K.M. *et al. Cell* **157**, 611–623 (2014).
3. Stewart, M.P. *et al. Nature* **469**, 226–230 (2011).
4. Ingber, D. *Ann. Med.* **35**, 564–577 (2003).
5. Bao, G. & Suresh, S. *Nat. Mater.* **2**, 715–725 (2003).
6. Mofrad, M.R.K. & Kamm, R.D. *Cytoskeletal Mechanics* (Cambridge Univ. Press, 2006).
7. Ng, L. *et al. J. Biomech.* **40**, 1011–1023 (2007).
8. Lam, W.A., Rosenbluth, M. & Fletcher, D. *Blood* **109**, 3505–3508 (2007).
9. Guck, J. *et al. Biophys. J.* **81**, 767–784 (2001).
10. Evans, E. & Yeung, A. *Biophys. J.* **56**, 151–160 (1989).
11. Otto, O. *et al. Nat. Methods* **12**, 199–202 (2015).
12. Mason, T.G., Ganesan, K., vanZanten, J.H., Wirtz, D. & Kuo, S.C. *Phys. Rev. Lett.* **79**, 3282–3285 (1997).
13. Yap, B. & Kamm, R. *J. Appl. Phys.* **98**, 1930–1939 (2005).
14. Panorchan, P., Lee, J., Kole, T., Tseng, Y. & Wirtz, D. *Biophys. J.* **91**, 3499–3507 (2006).
15. Dil, J.G. *Rep. Prog. Phys.* **45**, 285–334 (1982).
16. Scarcelli, G. & Yun, S.H. *Nat. Photonics* **2**, 39–43 (2008).
17. Eisenberg, S.R. & Grodzinsky, A.J. *J. Orthop. Res.* **3**, 148–159 (1985).
18. Scarcelli, G. & Yun, S.H. *Opt. Express* **19**, 10913–10922 (2011).
19. Zhou, E.H. *et al. Proc. Natl. Acad. Sci. USA* **106**, 10632–10637 (2009).
20. Barer, R. & Joseph, S. *Q. J. Microsc. Sci.* **95**, 399–423 (1954).
21. Scarcelli, G., Kim, P. & Yun, S.H. *Biophys. J.* **101**, 1539–1545 (2011).
22. Solon, J., Levental, I., Sengupta, K., Georges, P.C. & Janmey, P.A. *Biophys. J.* **93**, 4453–4461 (2007).
23. Ali, M.Y., Chuang, C.-Y. & Saif, M.T.A. *Soft Matter* **10**, 8829–8837 (2014).
24. Winer, J.P., Oake, S. & Janmey, P.A. *PLoS One* **4**, e6382 (2009).
25. Nijenhuis, N., Zhao, X., Carisey, A., Ballestrem, C. & Derby, B. *Biophys. J.* **107**, 1502–1512 (2014).

ONLINE METHODS

Brillouin scattering. Spontaneous Brillouin scattering arises from the interaction of light with acoustic phonons inside material. The Stokes frequency downshift occurs when light scattering generates an acoustic phonon. Anti-Stokes frequency upshift results when a photon gains energy from a phase-matched thermally generated acoustic phonon. In the approximation of an isotropic material in a probed voxel, the phase-matching acoustic frequency is given by $\Omega = 2K(M'/\rho)^{0.5}\sin(\theta/2)$, where K is the photon wavenumber, θ is the angle between incident and scattered photons, M' is the real part of the material longitudinal modulus and ρ is the mass density of the sample. In backward (epi-) detection, the frequency shift at the peak of the Brillouin spectrum is given at $\theta = \pi$ so that the real part of the longitudinal modulus is computed as $M' = \rho\lambda^2\Omega^2/(4n^2)$, where λ is the wavelength of the incident radiation and n is the index of refraction (**Supplementary Note 1**).

Confocal microscope. The light source of the Brillouin confocal microscope is a frequency-doubled Nd-YAG laser (Torus, Laser Quantum, Inc.) emitting a single longitudinal mode at 532 nm. The laser beam was cleaned with a single-mode spatial filter composed of a lens with a numerical aperture (NA) of 0.1 and a pinhole (Newport) with a hole size matched to the diffraction limit of the beam focus, recollimated and expanded with a lens of 125-mm focal length to overfill the back-aperture of the objective lens and inserted into an IX-71 microscope (Olympus). We cleared the optical path in the right-side port of the microscope and inserted a 100% reflection mirror just below the filter-cube turret. This mirror reflected the laser beam to the sample through an empty slot of the turret and directed the Brillouin light backscattered from the sample out of the microscope through the same port. Light was focused onto the cell sample by an objective lens of NA 0.6 in epi-illumination, with spatial resolution of ~$0.5 \times 0.5 \times 2\ \mu m^3$. For calibration, we used a pair of automated shutters and reference materials (**Supplementary Fig. 3**). For 3D imaging, a Brillouin spectrum was acquired from each location in the sample, and then the sample was translated stepwise using three-axis motorized stages (Prior). Scattered light from the samples was collected by a single-mode optical fiber (460HP, Thorlabs), which also served as a confocal pinhole, and delivered to the apodized VIPA spectrometer (**Supplementary Fig. 2**). With 2–4 mW illumination power at the sample, it generally took 2–5 min to acquire a 2D frame, depending on the number of pixels. In these conditions, cell morphology was not affected during repeated measurements, and no apparent difference in mechanical properties was observed between fresh cells and cells that were imaged multiple times. At higher powers exceeding 10 mW, cells remained viable, but they tended to change their shape after the imaging session.

VIPA spectrometer. The spectrometer consisted of two apodized cross-axis VIPA stages with a relay telescope and square-hole spatial filter between them (**Supplementary Note 2**). The two VIPA etalons had identical specifications (R1 = 99.9%, R2 = 95%, 1.6° internal tilt, Light Machinery). Linearly variable intensity filters (Rugate and Newport 50FS04DV) were used for apodization. The diffraction pattern after the final VIPA stage was detected with an electron-multiplying charge-coupled device (EM-CCD) camera (Ixon Du197, Andor) with a dispersion slope of 0.3 GHz/pixel.

Data acquisition and analysis. We used LabView for instrument automation, using modified manufacturer sample codes (Prior translational stages, Andor camera) and home-written codes to operate shutters. We used Matlab for spectral analysis. Our algorithm (provided as **Supplementary Software**) extracts the optical spectrum and measures the Brillouin shift and magnitude by curve-fitting with Lorentzian profiles (**Supplementary Fig. 3**). Brillouin images were produced in Matlab, typically using the "jet" colormap with red replaced by magenta. To quantify the average Brillouin shift of a cell, we typically acquired several *en face* sections of the cell under examination at different heights (similarly to **Fig. 2e**). After the measurement, we identified the voxels to average (i.e., belonging to the cell rather than the surrounding medium) using a threshold on Brillouin shift and linewidth.

Cell culture on 2D substrates. An NIH 3T3 fibroblast cell line tested for mycoplasma contamination was purchased from American Type Culture Collection (ATCC); after purchase, cells were frozen at early passage, and a fresh cell culture was routinely started from frozen stock. We maintained the cells and inspected them daily under an inverted-phase microscope to compare their morphology at different cell densities against reference images. Cells were grown on custom-made 2D substrates consisting of a collagen-coated polyacrylamide gel layer attached to 20-mm glass-bottom dishes. Glass-bottom dishes were first treated with 200 µl of (3-aminopropyl)trimethoxysilane for 3 min and 400 µl of 0.5% glutaraldehyde solution for 30 min to condition the glass for attachment to polyacrylamide. We then deposited 15–30 µl of polyacrylamide solution with 5–12% acrylamide and 0.04–0.4% bis-acrylamide in each glass well to create 50–100-µm-tall gels. Circular coverslips treated with Rain-X (ITW Global Brands) were placed face-down on the gel to create a flat, even surface. After the gels had solidified, the coverslips were discarded and the gels were treated with 1 ml of hydrazine hydrate for 4 h, followed by 2 ml of 5% glacial acetic acid for 1 h to allow attachment of collagen (type I from rat-tail) to the polyacrylamide gel. Gels were then washed with PBS three times for 30 min each time, sterilized under UV light and left overnight under a layer of 1.5 mg/ml oxidized collagen[26]. Gels were then washed in serum-free Dulbecco's modified Eagle's medium (DMEM) three times for 30 min each time and left in DMEM for at least 24 h before cell plating. Cells were plated on the gel substrate in DMEM supplemented with 10% FBS and allowed to spread for at least 24 h before imaging.

Osmotic pressure experiments. Hyperosmotic environments of varying strength were imposed on cells by the addition of 2× strength sucrose solutions of 0, 150, 300 or 500 mOsm in equal volume to the existing cell media. We made sucrose solutions by dissolving sucrose in DMEM supplemented with 1% FBS and sterilizing it for 30 min under UV light. Cells were grown on polyacrylamide gels, and the cell media was switched to DMEM supplemented with 1% FBS at least 6 h before sucrose was added or overnight. Cell stiffness was measured before and immediately after sucrose addition with Brillouin microscopy and with AFM for comparison. To supplement AFM measurements, we obtained average cell dimensions using confocal microscopy (**Supplementary Note 6**).

AFM-based micro-indentation. An Asylum MFP3D atomic force microscope (Asylum Research, Santa Barbara, CA) was used to perform the nanoindentation on single fibroblasts that were adhered to the polydimethylsiloxane-coated substrate. The cells were indented by gold-coated polystyrene colloidal probe tips (end radius $R \sim 2.5$ μm) attached to cantilevers with a nominal spring constant $k \sim 0.06$ N/m (Novascan, Ames, IA). We applied the thermal noise oscillation method to determine the cantilever spring constant for each probe tip[27]. The indentation was performed under a force control scheme, with a maximum force of ~2.5 nN. The resulting indentation depths were in the range of 0.2–1 μm. The axial (*z*-direction) displacement of the tip was calculated as the *z*-piezo subtracted from the vertical deflection of the cantilever. Typical force-displacement curves for cells in different sucrose concentrations are shown in **Supplementary Figure 7**. A typical force-displacement curve and the best-fit curve from the thin-layer Hertz model are shown in **Supplementary Figure 8**. We indented different locations on cells to obtain an average for the Young's modulus of each cell. An indentation speed of 0.1 μm/s was used to probe the Young's modulus under close-to-equilibrium conditions.

Reconstituted actin gel polymerization and branching. Branching F-actin was polymerized on polystyrene spheres precoated with *Viscum album* L. *var. coloratum* agglutinin (VCA), according to the protocol outlined by Pujol *et al.*[28]. An actin polymerization kit, VCA-Domain WASP protein, ARP2/3 protein, cofilin and gelsolin were all obtained from Cytoskeleton and handled according to the provided instructions. 4.5-μm carboxylated polystyrene spheres (Spherotech) were coated in VCA and added to actin buffer solution to polymerize the actin at 6.5 μM actin, 6.5 μM cofilin, 90 nM gelsolin, 180 nM ARP2/3 and 0.01% VCA. To stop polymerization, we diluted the actin solution 1:10 with 6.6-μM phalloidin. Beads were allowed to settle on a gel substrate to reduce motion and were imaged immediately thereafter. We also imaged the beads with confocal microscopy, for which we modified the dilution step to include 10% Alexa Fluor 594 phalloidin (Life Technologies).

Actin disruption via cytochalasin D. We achieved actin-filament disruption in NIH 3T3 cells by submerging cells in 5 μg/ml cytochalasin D (Sigma-Aldrich) in DMEM supplemented with 1% FBS. Cells were plated in DMEM supplemented with 10% FBS at least 24 h before imaging, and cell media was switched to DMEM supplemented with 1% FBS at least 6 h before to serum starve the cells and reduce cell movement during imaging. Cells were imaged 30 min to 1 h after the addition of a stock solution of cytochalasin made in DMEM.

Cell culture in 3D collagen gels. Rat tail collagen type I in acetic acid (BD Biosciences) was buffered with 10× PBS with phenol red, titrated to a pH of 8.0 with 0.1 M sodium hydroxide, and brought to a final concentration of 2 mg/mL with water. Cells were lifted from culture with Trypsin-EDTA, centrifuged at 200*g* for 5 min, resuspended in growth medium and mixed with collagen I solution for a final concentration of 4×10^5 cells per milliliter of total collagen solution. Collagen was polymerized in humidified chambers at 37 °C and 5% CO_2 for 20 min before growth medium was added to hydrate the gel.

Dependence of cell stiffness on spread area. To quantitatively assess the cell stiffness–morphology relationship, we measured the average cell stiffness versus the projected cell area for several conditions. For each cell, we estimated the Brillouin shift by averaging the frequency shift at each pixel in the cell; we estimated the projected cell area by determining the cell contour from the phase-contrast image and computing the enclosed area with ImageJ. In the 3D cultures, only cells with extended morphology were analyzed, and round cells were discarded. In plots, each data point corresponds to a different cell. The points were fit to the same linear regression curve ($R > 0.8$, $P < 0.001$).

Code availability. The Matlab code used to analyze data is provided as **Supplementary Software** along with representative **Supplementary Data** to run the code.

26. Damljanović, V., Lagerholm, B. & Jacobson, K. *Biotechniques* **39**, 847–851 (2005).
27. Hutter, J.L. & Bechhoefer, J. *Rev. Sci. Instrum.* **64**, 1868 (1993).
28. Pujol, T., du Roure, O., Fermigier, M. & Heuvingh, J. *Proc. Natl. Acad. Sci. USA* **109**, 10364–10369 (2012).

doi:10.1038/nmeth.3616

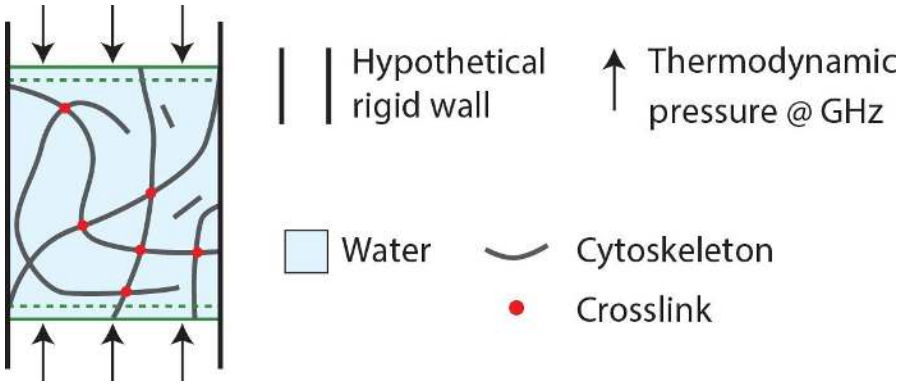

Supplementary Figure 1

Longitudinal modulus.

Illustration of cytoplasm, axial stress and axial compression of the medium. The ratio of stress to strain defines the longitudinal modulus. The Brillouin frequency shift is related to the local longitudinal modulus of the medium.

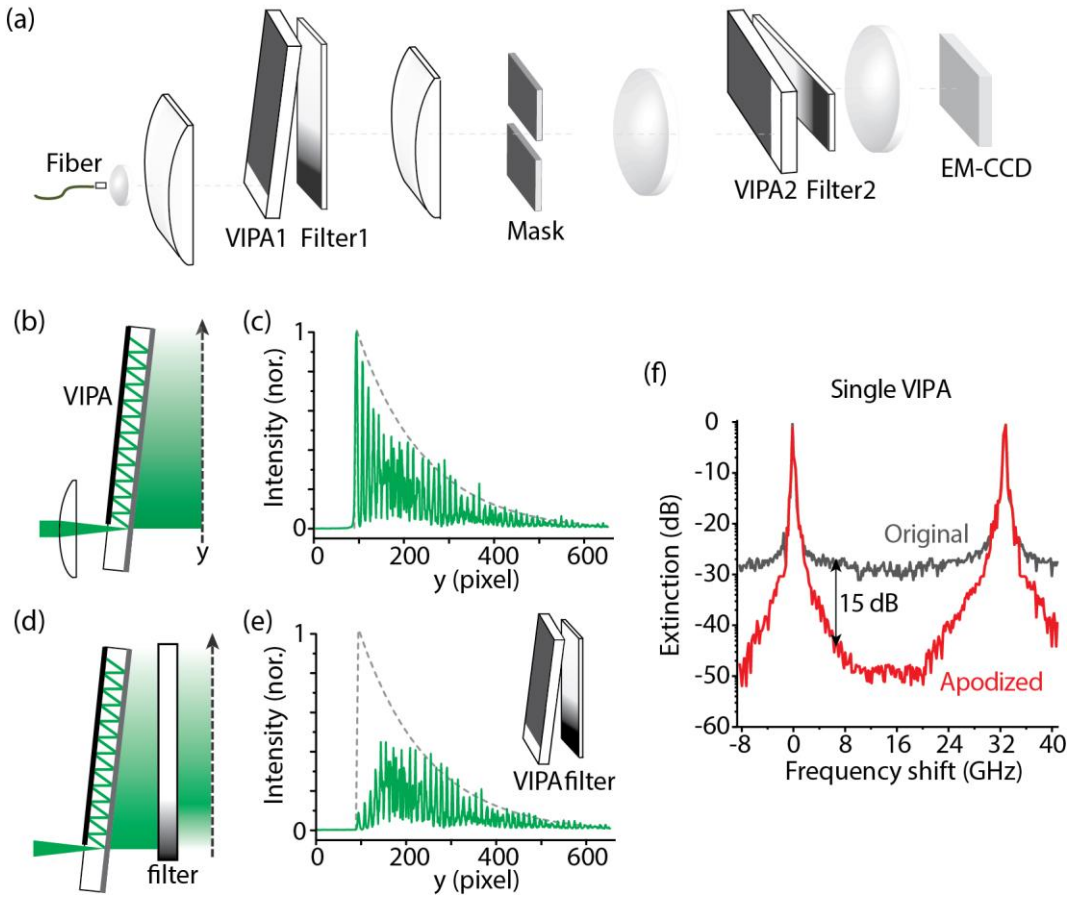

Supplementary Figure 2

Apodized VIPA spectrometer.

(**a**) Schematic of the double-stage apodized VIPA spectrometer. (**b**) As a result of multiple reflections within the etalon, the beam output from the VIPA has an exponential profile. (**c**) Measured VIPA output beam profile (solid lines) shows an exponential envelope. (**d**) The gradient intensity filter converts the exponential profile to an apodized beam shape that has reduced high spatial-frequency components. (**e**) Measured VIPA output beam profile (solid lines) compared to the exponential envelope without the filter (dotted line). (f) The resulting spectrum shows increased spectral extinction by ~15 dB at 7.5 GHz away from the elastic scattering peaks and >20 dB in a frequency band between 8 and 20 GHz.

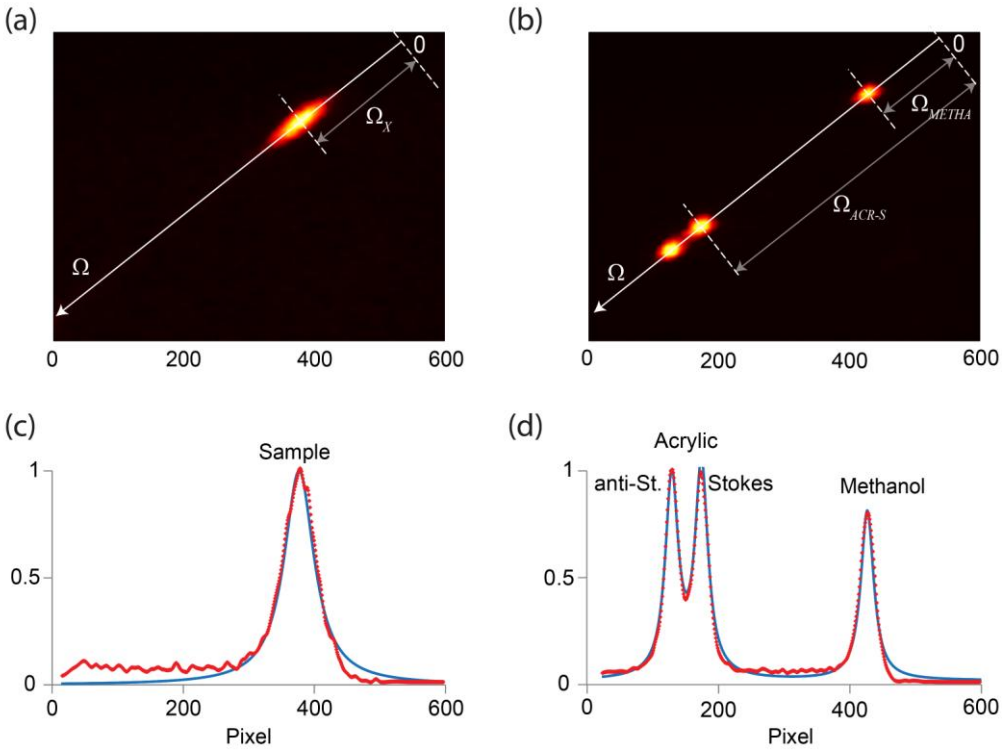

Supplementary Figure 3

Calibration and analysis of Brillouin spectrum.

Spectrometer calibration. (**a**) CCD frame obtained from a sample. (**b**) CCD frame from two reference materials. (**c**,**d**) Lorentzian curve fit (blue) to the measured data (red). Ω_X is determined from $\Omega_{ACR\text{-}S}$ and $\Omega_{METHA.}$

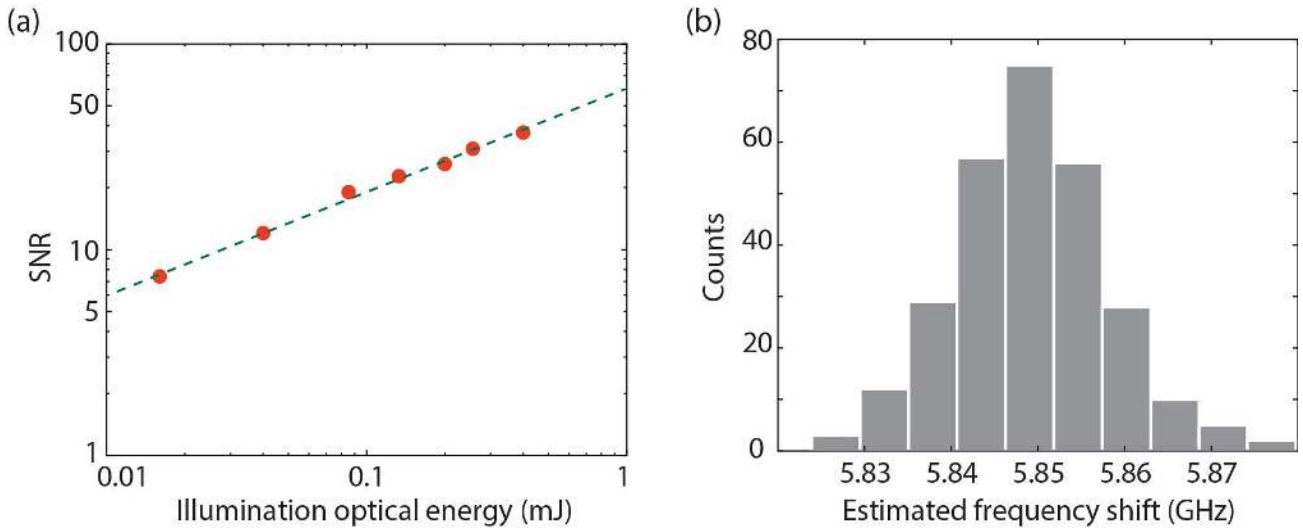

Supplementary Figure 4

Accuracy of Brillouin-shift estimation.

(**a**) Logarithmic plot of the instrument SNR versus the total number of photons collected (proportional to the product of illumination power and acquisition time). Circles: measurement data; dotted line: linear fit. (**b**) Representative distribution of Brillouin shifts estimated from $N = 300$ sequential spectra of a methanol sample recorded at 4 mW and 50 ms.

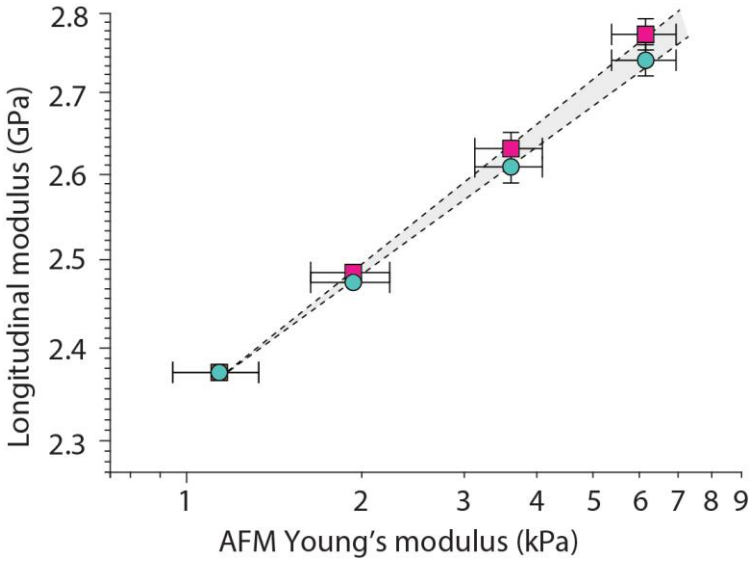

Supplementary Figure 5

Computation of longitudinal modulus.

Brillouin-measured longitudinal modulus versus AFM-based Young's moduli of NIH 3T3 fibroblast cells at different osmotic pressure conditions. The magenta dots take into account the variation of ρ/n^2 between the samples; the turquoise dots assume constant ρ/n^2. Lines are linear fits.

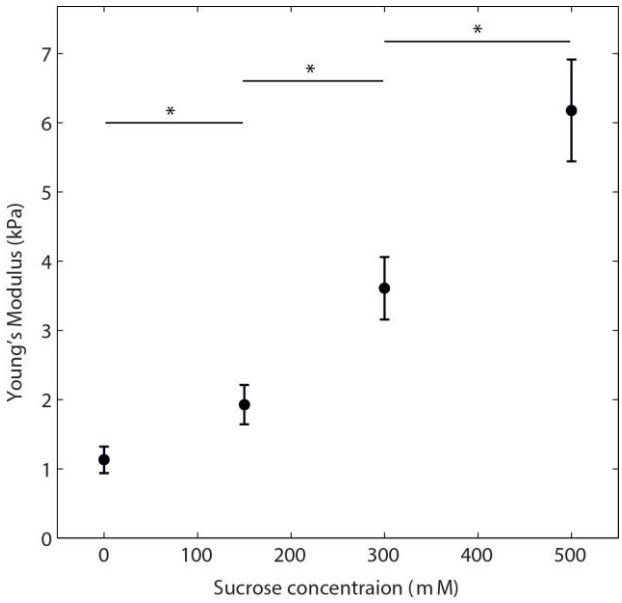

Supplementary Figure 6

AFM-based micro-indentation to estimate Young's modulus.

The Young's modulus of fibroblasts was measured via AFM-based indentation in different sucrose concentrations (mean ± s.e.m.; number of cells per concentration $N \geq 8$; the Young's modulus of each cell is the average of the Young's modulus at $M \geq 4$ indentation sites; $^{*}P < 0.05$ using *t*-test).

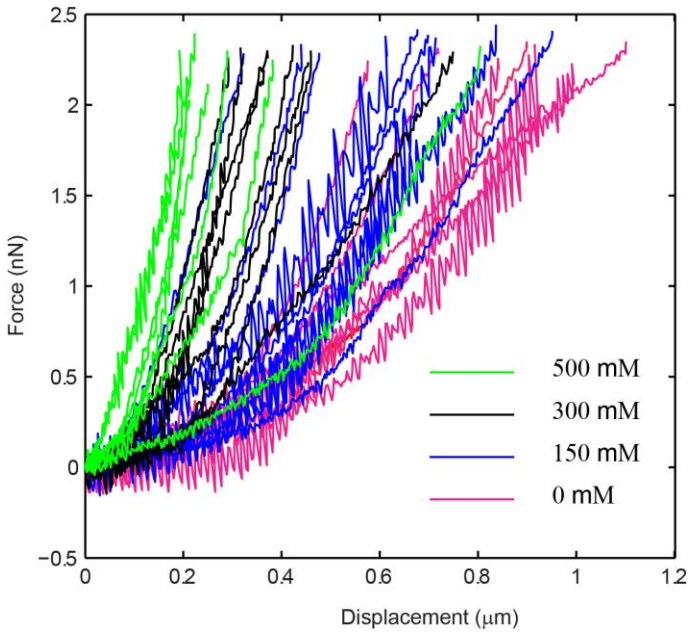

Supplementary Figure 7

AFM force-displacement curves.

The force-displacement curves for cells at different concentrations of sucrose in the cell medium.

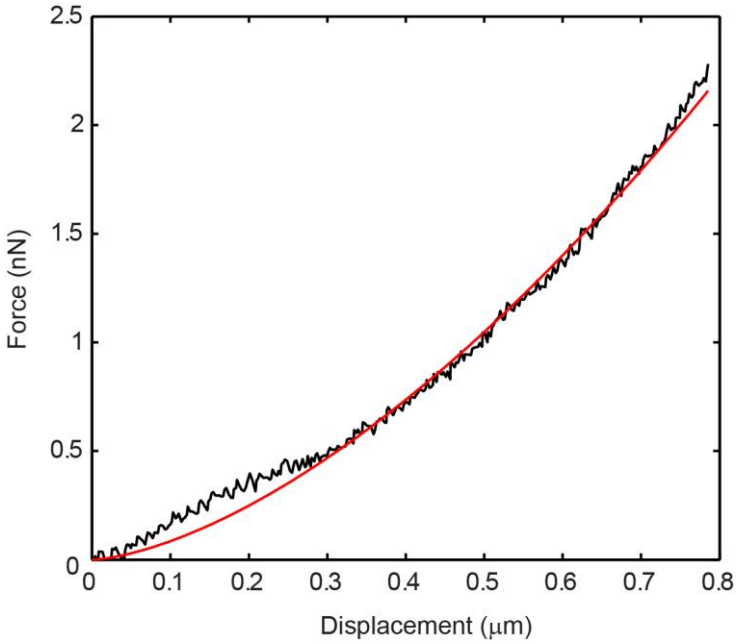

Supplementary Figure 8

Hertz model fit of AFM indentation.

A typical force-displacement curve (black) and the corresponding best fit curve (red) from the thin-layer Hertz model are shown for a cell in 300 mM sucrose.

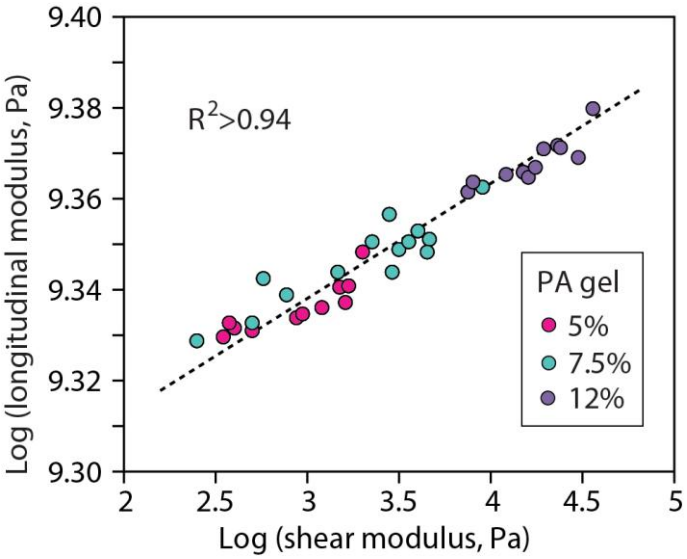

Supplementary Figure 9

Brillouin-mechanical validation in polyacrylamide gels.

A log-log linear relation of the longitudinal modulus and shear modulus of polyacrylamide (PA) gels. The measurement data are for cross-linked PA gels at three different polymer concentrations (5%, 7.5%, 10% wt) and several concentrations of bis-acrylamide cross-linker (0.1–0.6% wt).

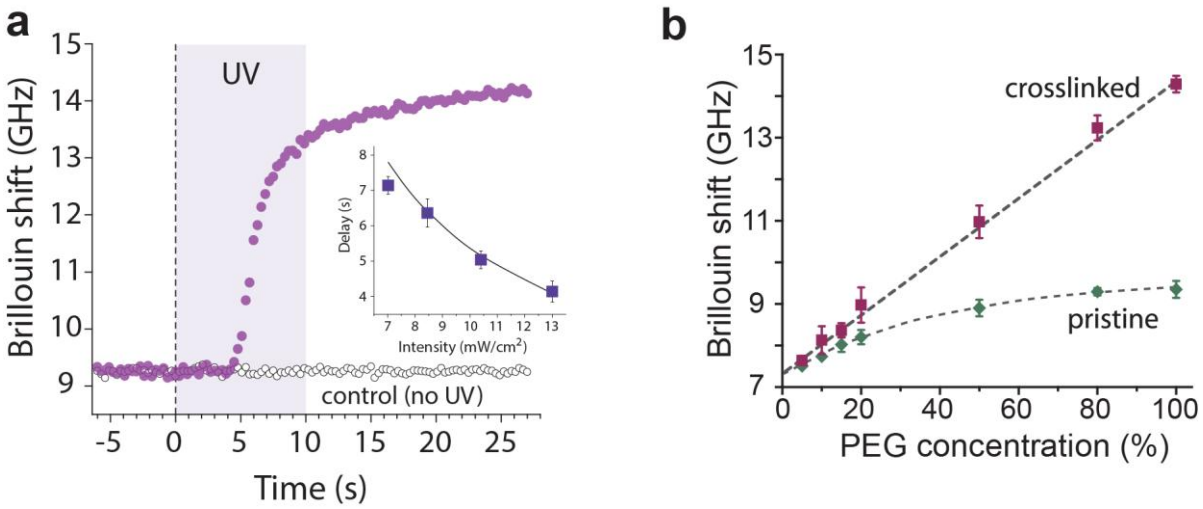

Supplementary Figure 10

In situ measurement of PEG hydrogel cross-linking.

(**a**) Real-time monitoring of photopolymerization induced by UV light illumination (0–10 s), which reveals a delayed onset of polymerization (4 s) and increased degree of cross-linking during and after illumination. Control, without UV illumination. Inset, polymerization induction time at various UV power levels; circles, experimental data; dashed line, theoretical model. (**b**) Brillouin shift of PEG at various concentrations before (squares) and after (diamonds) photopolymerization. Error bars, s.e.m. ($N = 10$).

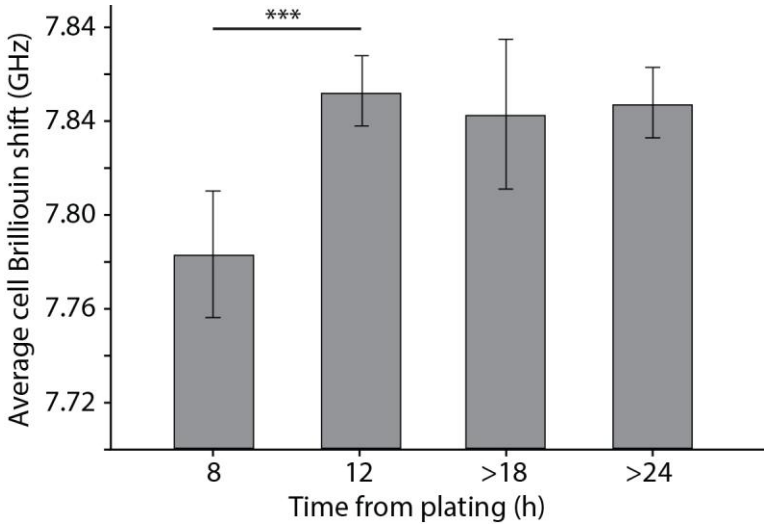

Supplementary Figure 11

Brillouin shift of cells at different plating times.

Average Brillouin shift of NIH 3T3 fibroblasts cultured on top of polyacrylamide gels and measured 8 h after plating time ($N = 6$) and 12 h after plating time ($N = 3$). For comparison, cells measured 18 h ($N = 8$) and 24 h ($N = 12$) after plating are shown.

Supplementary Note 1: Longitudinal modulus

Longitudinal modulus is defined as the ratio of uniaxial stress to uniaxial strain (**Supplementary Fig. 1**) with zero transverse strain. A longitudinal acoustic wave involves such longitudinal stress and strain. In Brillouin interactions in the GHz frequency range, we probe the longitudinal modulus by measuring thermodynamically generated acoustic vibrations within the probed voxel. In the quasi-static limit, the longitudinal modulus, *M*, is related to the bulk modulus, *K*, and shear modulus, *G*, as follows: $M=K+4/3G$. The bulk modulus has little frequency dependence; on the other hand, shear and Young's moduli have been shown to increase significantly with frequency[1]. In Brillouin measurements, we expect a strong contribution of the bulk modulus of water as modified by the presence of other macromolecules in the cell microenvironment.

For viscoelastic materials, these moduli are complex quantities. The real part, the storage modulus, accounts for the elastic behavior (stored elastic energy), and the imaginary part, the loss modulus, describes the viscous-like dissipation (associated with rate processes within the solid network alone and/or fluid flow with respect to the porous solid network[2]). The Brillouin frequency shift as previously described is given by $\Omega=2K\sqrt{M'/\rho}\sin(\theta/2)$, with K the photon wavenumber, θ the angle between incident and scattered photons, M' the real part of the material longitudinal modulus and ρ the mass density of the sample; it is therefore proportional to the propagation velocity $\sqrt{M'/\rho}$ of the gigahertz acoustic waves inside the material.

In principle, both longitudinal and shear moduli at GHz can be probed by Brillouin spectroscopy. However, the measurement of shear modulus requires the detection of scattered light at a 90-degree angle in the polarization state orthogonal to the input polarization state. Furthermore, the strength of shear Brillouin scattering is much lower than longitudinal Brillouin scattering in most materials and should be negligible for cytoplasms due to their high water content.

Supplementary Note 2: Apodized VIPA spectrometer

We have previously demonstrated a double stage spectrometer for high throughput analysis of Brillouin scattering[3]. Here, we introduce a novel apodization technique to improve the spectral contrast (or extinction) of the spectrometer (**Supplementary Fig. 2a**). Virtually Imaged Phased Array (VIPA)[4] is a modified tilted Fabry-Perot etalon to which cylindrically focused light is coupled through a narrow anti-reflection coated window. Upon entering the etalon, light undergoes multiple internal reflections and the multi-beam interference induces high spectral dispersion; a Fourier transform lens then focuses the pattern on the detector. Because of the multiple partial reflections, light from a VIPA etalon exits with an exponential intensity profile along the dispersion direction (**Supplementary Fig. 2b-c**). The Fourier transform lens then focuses the exponential beam into a Lorentzian transverse profile. This Lorentzian spectral transfer function carries significant energy at the wings compared to a Gaussian profile. Considering a VIPA with a finesse of 40, the magnitude of the wing with respect to the peak transmission is about −30 dB. This extinction ratio is not sufficient to reject back-reflections or stray light in Brillouin cellular microscopy.

To improve the extinction, one of the effective strategies is to convert the exponential beam profile to a Gaussian profile. To accomplish this, we used an apodization filter that converts the exponential beam profile to a more rounded shape (**Supplementary Fig. 2d**). For this, we used a linear-variable neutral density filter (Rugate Inc, or Newport 50FS04DV). This device provided a steep transmission slope to smoothen the sharp edge of the exponential profile. The effective apodization is clearly seen in the output beam profile as imaged from the

output face of the etalon (**Supplementary Fig. 2e**, solid vs. dotted line). With the filter, extinction in the transfer function was measured to be greater than -40 dB (**Supplementary Fig. 2f**, red), improved from −30 dB before apodization (**Supplementary Fig. 2f**, black). This result agreed well with our calculation based on the measured beam profiles.

Supplementary Note 3: Calibration and analysis of Brillouin spectrum

We implemented *in situ* calibration of the spectrometer free spectral range (FSR) and the CCD-pixel to optical-frequency conversion ratio (PR) in the Brillouin microscope. To determine these parameters, we fitted the setup with two calibration arms carrying reference materials with known Brillouin shifts. These could be interrogated periodically using a pair of computer-controlled motorized shutters.

In our procedure for calibration and spectral analysis, we first consider a CCD frame captured from a sample to be measured (**Supplementary Fig. 3a**). Switching the probe light to the calibration arm, a frame exhibiting two distinct peaks corresponding to Methanol and Acrylic (both Stokes and anti-Stokes peaks of the acrylic are seen) is observed (**Supplementary Fig. 3b**). It can be shown that:

$$\frac{FSR}{2} - PR \bullet \left[P_{ACR-S} - \left(\frac{P_{ACR-S} + P_{ACR-AS}}{2} \right) \right] = \Omega_{ACR-S}$$

$$\frac{FSR}{2} - PR \bullet \left[P_{METHA} - \left(\frac{P_{ACR-S} + P_{ACR-AS}}{2} \right) \right] = \Omega_{METHA}$$

where $P_{ACR\text{-}S}$, $P_{ACR\text{-}AS}$ and P_{METHA} denote the measured value of Brillouin peaks in pixel units and $\Omega_{ACR\text{-}S}$ and Ω_{METHA} represent the actual value of Brillouin peaks in GHz units. These equations can be solved for the two unknowns, FSR and PR.

The Brillouin peak in pixel units P_X is measured by Lorentzian curve fitting. Then, the Brillouin shift of sample, Ω_X, is calculated from the following expression:

$$\Omega_X = \frac{FSR}{2} - PR \bullet \left[P_X - \left(\frac{P_{ACR-S} + P_{ACR-AS}}{2} \right) \right].$$

The wavelength of acoustic phonons in water and cytoplasm is about 200 nm, which is equal to one half of the optical wavelength (532 nm / 1.33 / 2 = 200 nm). From this, the propagation speed of an acoustic phonon is determined to be 200 nm x 7.5 GHz = 1,500 m/s. The measured Brillouin spectrum has a Lorenzian profile with a spectral width of about 500 MHz in both water and cytoplasm at 37 °C. This finite linewidth is due to the damping of acoustic phonons.

Supplementary Note 4: Accuracy of Brillouin shift estimation

In Brillouin scattering spectroscopy, the induced frequency shift, Ω, is related to the longitudinal modulus M', through the relation $M'=\rho\lambda^2\Omega^2/(4n^2)$, where ρ is the mass density, λ is the optical wavelength and n is the refractive index. Thus, the ability of the instrument to detect changes in longitudinal modulus, $\Delta M'$ is related to the measurement accuracy of the Brillouin frequency shift, $\delta\Omega$. Thanks to the apodized design, our Brillouin spectrometer is background-free, and operated in the shot noise limited regime. In this regime, the accuracy in the determination of the center of the Brillouin spectrum is ultimately limited by the signal-to-noise ratio (SNR) according to the relation[5]:

$$\delta\Omega = \frac{\sqrt{\Delta_{\mathrm{B}}^2 + \Delta_{\mathrm{NA}}^2 + \mathrm{p}^2/12 + \mathrm{r}^2}}{SNR}$$

where Δ_{B} is the intrinsic linewidth of the Brillouin spectrum; Δ_{NA} is the broadening due to high-NA collection; p is the pixel spectral dispersion, i.e. the frequency interval between two adjacent CCD pixels in the spectrometer (~0.15 GHz); r is the spectral resolution, determined by the Free Spectral Range (FSR=20GHz) divided by the finesse of the spectrometer (~40). In the epi-illumination epi-detection configuration, signal collection is maximal while spectrum broadening due to high-NA is minimal due to the cosine angle dependence of Brillouin shift. We verified experimentally that NA-induced linewidth broadening does not prevent accurate measurements: the overall spectral linewidth was measured to be ~0.55 GHz at NA=0.6, and ~0.63 GHz at NA=1.4, only marginally increased with respect to the intrinsic instrumental linewidth of ~0.5 GHz measured at low NA.

To verify shot-noise limited operation, we measured the SNR at different illumination power levels and spectrum acquisition times. Brillouin spectra of methanol were acquired at different power levels ranging 1.5 mW and 4 mW and different acquisition times ranging from 4 ms to 100 ms. A good square root dependence of SNR on the product of acquisition time and power level demonstrating shot-noise limited operation (**Supplementary Fig. 4a**). An exemplary distribution of estimated shifts is shown for the 50 ms acquisition time and 4 mW power settings (**Supplementary Fig. 4b**). The standard deviation of this distribution can be used to estimate the accuracy in peak localization, in this case it is 8.8 MHz, or 0.15% as reported in the main text. Also the experimental accuracy in peak localization showed a good square root dependence on collected number of photons. Peak localization accuracy agreed well with Eq. (1) and was measured to be inversely proportional to SNR, yielding 4 MHz/mW/√Hz. This relationship allows us estimating the sensitivity of our technique to elasticity changes within the cell: differentiating, we get $\Delta M'/M' = a\Delta E'/E'$, where $\Delta M'$ and $\Delta E'$ are variation of longitudinal and Young's moduli and the coefficient a is typically found in the range of 0.02 to 0.1 in cells, tissues and biopolymers[6]. Thus, a Brillouin frequency sensitivity of 0.1% corresponds to a relative error in longitudinal modulus of $\Delta M'/M' \approx 0.2\%$, which indicates that the instrument is able to detect changes $\Delta E'/E'$ as little as 2 to 10%.

Supplementary Note 5: Computation of longitudinal modulus

To derive the longitudinal modulus from the Brillouin spectral shift, through the relation $M' = \rho\lambda^2\Omega^2/(4n^2)$, the ratio of density to index of refraction ρ/n^2 needs to be estimated. Both density and index may vary spatially within a cell and from condition to condition, however, their ratio is found to be approximately constant[7]. We use the osmotic pressure experiments to validate this consideration (**Supplementary Fig. 5**). In the main text (**Fig. 1e**), we showed the correlation between micro-indentation Young's modulus, and longitudinal modulus computed using constant values for density (1.08 g/cm^3) and index (1.37). This curve is reproduced in **Supplementary Fig. 5** with turquoise dots. For comparison, in magenta, we also show the estimated values of longitudinal modulus using density and refractive index values derived from the volume changes induced by osmotic pressure as calculated by the Boyle-Van't Hoff equation[8]. Even at the highest osmotic pressure condition, the two estimations of longitudinal modulus differ by ~1%, which demonstrates how the longitudinal modulus can be effectively computed directly from Brillouin shift.

Supplementary Note 6: AFM-based micro-indentation to estimate Young's modulus

The AFM micro-indentation test provides a force-vs-elongation curve, which can be used to extract the overall mechanical properties of the cell. The Young's modulus of cells was obtained by using the thin-layer Hertz model[9]:

$$F = \frac{4E_Y R^{1/2}}{3(1-\nu)}\delta^{3/2}\left[1 - \frac{2\alpha_0}{\pi}\chi + \frac{4{\alpha_0}^2}{\pi^2}\chi^2 - \frac{8}{\pi^3}\left({\alpha_0}^3 + \frac{4\pi^2}{15}\beta_0\right)\chi^3 + \frac{16\alpha_0}{\pi^4}\left(\alpha_0^3 + \frac{3\pi^2}{5}\beta_0\right)\chi^4\right]$$

where

$$\alpha_0 = -\frac{1.2876 - 1.4678\nu + 1.3442\nu^2}{1-\nu}$$
$$\beta_0 = \frac{0.6387 - 1.0277\nu + 1.5164\nu^2}{1-\nu}$$

and F is the applied force, δ is the indentation depth, E_Y is the Young's modulus, R is the probe radius, ν is the Poisson's ration, $\chi = \sqrt{R\delta}/h$, and h is the cell height. The force and indentation depth were obtained from force-displacement curves of AFM based indentation. In the model we used average cell height h = 7.5 µm for all conditions, estimated via high-resolution confocal fluorescence microscopy, by staining the plasma membrane. Fluorescence images were interpolated, thresholded and processed to identify cell edges and measure typical dimensions using ImageJ software. The Poisson's ratio was assumed to be ν = 0.4 based on previous studies on chondrocytes[10] and fibroblasts[11].
The overall results obtained from AFM micro-indentation are shown in **Supplementary Fig. 6**. The force-displacement curves for several cells in different sucrose concentrations are shown in **Supplementary Fig. 7**. Typical force-displacement curve and the best-fit curve from the thin-layer Hertz model are shown in **Supplementary Fig. 8**.

Supplementary Note 7: Brillouin-mechanical validation in polyacrylamide gels.

To further understand and validate the relationship between Brillouin-derived high-frequency longitudinal modulus and quasi-static traditional Young's or shear moduli, we have developed polyacrylamide (PA) gels of varying water content (5% to 12% polymer wt%) and varying bis-acrylamide concentrations (0.01% to 0.3% polymer wt%) to cover a range of substrate stiffness between ~600 Pa and 20 kPa that are generally used as a cell substrates[12]. Using these gels we have compared longitudinal modulus as measured with our Brillouin apparatus with shear modulus measured with a rheometer. Gels were generally created in 6-well plates; after gel polymerization the well-plates were placed under the Brillouin microscope and Brillouin shift values were recorded at different locations. High-frequency longitudinal moduli were computed from the Brillouin shift values using values of mass density and index of refraction computed from the composition of the gels. Then, a biopsy punch was used to extract disks (typically 3 disks per gel composition of 4 mm diameter, 2-5 mm height) from the polyacrylamide gels. To obtain the shear modulus, the PA disks were measured with an AR-G2 stress-controlled rheometer (TA Instruments) with 8-mm-diameter parallel plate geometry. We used 100 µm pre-compression, performed frequency sweeps from 0.1 to 10 Hz with 0.1% strain amplitude at 23°C and used the 1 Hz values for comparison with Brillouin. High correlation (R^2>0.94) was obtained in curve fit to a log-log linear relationship: $\log(M') = a\log(G') + b$, where the fitting parameters were a=0.023 and b=9.27 (**Supplementary Fig. 9**). Within this range of water content and crosslinker formulations, the effect of changing the water content within the gels or

increasing number of crosslinks leads to similar correlations between high-frequency longitudinal modulus and quasi-static shear modulus, thus demonstrating that our method is sensitive to changes in polymer concentration and crosslinking.

Supplementary Note 8: Brillouin shift of cells at different plating times

After plating cells into a culture dish, cells undergo a slow process that starts with attachment onto the substrate and ends with the cells fully spread. During this time, cells progressively change their morphology from round in suspension to stretched onto a substrate. In this process, the projected cell area grows and the actin cytoskeleton polymerizes. To investigate the cell internal stiffness as a function of time from plating, we plated NIH 3T3 fibroblasts onto polyacrylamide gels (12%) functionalized with collagen (see **Online Methods**). We measured several conditions starting at 8 hours after plating. We chose this time point because at earlier time points strong variations in the nucleus to cytoplasm volume may bias the measurements. A highly statistically significant difference (unpaired t-test, $p<0.001$) was observed between the 8-hour and 12-hour conditions (**Supplementary Fig. 11**), indicating that as cells grow and stabilize their cytoskeleton, also their internal stiffness increases, as one would expect. For comparison we also show the average value on cells plated by more than 18 hours and 24 hours, which indicates that after 12 hours the cells are fully spread and cell stiffness reaches a plateau value.

References

1. Fabry, B.*, et al.* Scaling the microrheology of living cells. *Physical Review Letters* **87**(2001).
2. Moeendarbary, E.*, et al.* The cytoplasm of living cells behaves as a poroelastic material. *Nature Materials* **12**, 253-261 (2013).
3. Scarcelli, G. & Yun, S. Multistage VIPA etalons for high-extinction parallel Brillouin spectroscopy. *Optics Express* **19**, 10913-10922 (2011).
4. Shirasaki, M. Large angular dispersion by a virtually imaged phased array and its application to a wavelength demultiplexer. *Opt. Lett.* **21**, 366-368 (1996).
5. Thompson, R.E., Larson, D.R. & Webb, W.W. Precise nanometer localization analysis for individual fluorescent probes. *Biophysical Journal* **82**, 2775-2783 (2002).
6. Scarcelli, G., Kim, P. & Yun, S.H. In vivo measurement of age-related stiffening in the crystalline lens by Brillouin optical microscopy. *Biophysical Journal* **101**, 1539-1545 (2011).
7. Scarcelli, G., Pineda, R. & Yun, S. Brillouin Optical Microscopy for Corneal Biomechanics. *Investigative Ophthalmology & Visual Science* **53**, 185-190 (2012).
8. Zhou, E.*, et al.* Universal behavior of the osmotically compressed cell and its analogy to the colloidal glass transition. *Proceedings of the National Academy of Sciences of the United States of America* **106**, 10632-10637 (2009).
9. Darling, E.M., Zauscher, S., Block, J.A. & Guilak, F. A thin-layer model for viscoelastic, stress-relaxation testing of cells using atomic force microscopy: do cell properties reflect metastatic potential? *Biophysical Journal* **92**, 1784-1791 (2007).
10. Ng, L.*, et al.* Nanomechanical properties of individual chondrocytes and their developing growth factor-stimulated pericellular matrix. *Journal of biomechanics* **40**, 1011-1023 (2007).
11. Mahaffy, R.E., Park, S., Gerde, E., Kas, J. & Shih, C.K. Quantitative analysis of the viscoelastic properties of thin regions of fibroblasts using atomic force microscopy. *Biophysical Journal* **86**, 1777-1793 (2004).
12. Fischer, R., Myers, K., Gardel, M. & Waterman, C. Stiffness-controlled three-dimensional extracellular matrices for high-resolution imaging of cell behavior. *Nature Protocols* **7**, 2056-2066 (2012).